Ceramics International 46 (2020) 1352–1361

Contents lists available at ScienceDirect

Ceramics International

journal homepage: www.elsevier.com/locate/ceramint

Effects of molten-salt processing parameters on the structural and optical properties of preformed $La_2Zr_2O_7:Eu^{3+}$ nanoparticles

Mitzy A. Penilla Garcia[a], Santosh K. Gupta[a,b], Yuanbing Mao[a,c,*]

[a] Department of Chemistry, University of Texas Rio Grande Valley, 1201 West University Drive, Edinburg, TX, 78539, USA
[b] Radiochemistry Division, Bhabha Atomic Research Centre, Trombay, Mumbai, 400085, India
[c] Department of Chemistry, Illinois Institute of Technology, 3105 South Dearborn Street, Chicago, IL, 60616, USA

ARTICLE INFO

Keywords:
Molten-salt process
Nanoparticles
Pyrochlore
$La_2Zr_2O_7:5\%Eu^{3+}$
Photoluminescence

ABSTRACT

Molten-salt method has been used to synthesize various functional materials, but it has not been employed to adjust the structure, particle size, and properties of preformed particles. To fill the knowledge gap, in this study, we use a molten-salt medium to reprocess preformed $La_2Zr_2O_7:5\%Eu^{3+}$ nanoparticles which were already formed by a molten-salt synthesis (MSS) method. The molten-salt processing is conducted under various conditions in terms of processing time, temperature, and medium. Specifically, within the studied molten-salt processing time (0 h–24 h) at 800°C, 3 h was found to offer the best optical output. In terms of the investigated molten-salt processing temperature (650 °C–1100 °C) for 3 h, 800 °C was identified as the most desirable annealing temperature. Regarding the explored molten-salt processing media (nitrate *vs.* chloride) at 3 h and 800 °C, better luminescence results were obtained for nanoparticles processed in chloride. Under each processing parameter, the change of optical properties is explained based on the balance among the crystalline size, crystal structure, crystallinity, defect, and agglomeration characteristics of the molten salt processed $La_2Zr_2O_7:5\%Eu^{3+}$ particles. We expect this study will excite other scientists to further explore molten-salt processing as an effective post-synthesis method to fine-tune the structure, particle size, and properties of preformed particles to meet the demand of functional materials.

1. Introduction

Nanostructured materials with large surface area and improved reactivity display superior optical, magnetic, catalytic, chemical, biological properties useful for various technological applications [1–3]. It is reported that particle size, crystallinity, and optical properties of nanoparticles are strongly affected by nucleation time, synthesis temperature, aging time, and post-synthesis treatment [4–7]. Through the addition of molten salts as a synthesis medium it is reported that metal oxide nanoparticles can be synthesized very rapidly and efficiently by reacting metal ion precursors along with suitable flux/molten salt at temperature above the melting point of the salts. This approach is known as molten salt synthesis (MSS) method [8,9]. In terms of molten-salt process as a synthesis technique, among various bottom-up synthesis approaches, it has been widely used to synthesize nanomaterials with various compositions since it is facile, low temperature (compared to conventional solid-state synthesis), and environmentally benign [10–17]. Compared to other synthesis techniques, the MSS method reduces the product formation temperature as the added molten salt aids in rapid movement of reactant species through convection and diffusion [14,15,17–19]. This method also displays unique advantage towards NP synthesis such as simple to operate [20], facilitate large scale production [19], cost effective [21], low defect [21,22], ligand free surface [22], reproducible [17], and environmentally friendly [23,24]. The most fascinating aspects of the MSS method which makes it highly environmentally friendly is the high water solubility of most of the molten salt. It not only facilitates the easy removal but makes very efficient isolation of final products at the end of chemical reaction and synthesis. It was also found to be highly successful in solvating most of the metallic ions at slightly enhanced temperature unlike other wet chemical routes. This is ascribed to destabilization of most of metal ions or covalent/ionic bonds through strong polarization induced by molten salt and its ions at high temperature. It is reported that even some complex oxides which remain insoluble in hydrothermal synthesis media can be solubilized using molten salt. It is observed by various researchers that exposing nanoparticle to high annealing time and temperature induce particle growth through Ostwald ripening which have strong influence on its optical particles [18,25,26]. Such thermal

* Corresponding author. Department of Chemistry, University of Texas Rio Grande Valley, 1201 West University Drive, Edinburg, TX, 78539, USA.
E-mail address: ymao17@iit.edu (Y. Mao).

https://doi.org/10.1016/j.ceramint.2019.09.098
Received 25 June 2019; Received in revised form 4 September 2019; Accepted 11 September 2019
Available online 12 September 2019

treatment is also expected to affects crystallinity, defects, surface area, etc. which have strong impact on the emission kinetics, photo and radioluminescence of nanomaterials [25,27,28]. Earlier it was also observed that powder characteristics is affected strongly by MSS processing time, temperature, co-precipitating pH and type of salt used [18,25,26,29–37]. The MSS method is somewhat comparable to combustion synthesis where fuel is added and reaction is facilitated by nature and amount of fuel (e.g. urea, glycine, ascorbic acid, etc.) and heat of combustion [38–40]. On the other hand, molten salt is used in the MSS method and product quality and reaction temperature are governed by the eutectic point of molten salt used, such as $NaNO_3$–KNO_3, NaCl–KCl, etc. Moreover, there are a few reports wherein materials are synthesized by molten-salt assisted combustion synthesis [41].

It is known that post-synthesis thermal treatment of preformed materials affects their properties, e.g. optical properties of nanomaterials, likely by affecting defect concentration, crystallinity, surface area, degree of aggregation, etc. [18,25,26,30] It is reported that post-synthesis thermal treatment to tailor material properties have been and will continue to be indispensable to realize emerging and to improve conventional applications [31]. There are several post-synthesis treatment processes of advanced materials to tune their functional properties such as thermal activation, chemical activation, doping, functionalization, metal deposition, isomorphous substitution, demetallation, tribochemical treatment, etc. [31–33,42] This can also lead to changes of their type, size and density of defects. The widening window of post-synthesis treatment options of functional materials enables the preparation of pyrochlore with application-specific properties [34–37]. However, regarding it as a post-synthesis treatment method, to the best of our knowledge, molten-salt process has not been employed to adjust the structure, particle size, and properties of preformed particles, especially those pre-synthesized by molten-salt method. Specifically, until now, there has been no report on the post-synthesis thermal treatment and the investigation of the photoluminescence of europium doped lanthanum zirconate $La_2Zr_2O_7$:Eu^{3+} (LZOE) nanoparticles (NPs) preformed by the MSS method.

$A_2B_2O_7$ type compounds are a diverse class of oxides with broad technological applications [17,34,37,43]. They exist in two main phases of disordered fluorite (DF) and ordered pyrochlore (OP). The difference arises due to the position of oxygen in the crystal lattice. In OP, the oxygen atoms will occupy specific sites in the lattice (48f and 8b) whereas in DF the oxygen atoms are arranged randomly throughout the lattice. Among $A_2B_2O_7$ type compounds, $La_2Zr_2O_7$ has fascinating properties with broad applications for solid-state lighting [44], scintillators [44], nuclear waste host [45], thermal barrier coatings [46], thin film transistors [47], fuel cells [48], etc.

On the expected line to see the implication of molten-salt processing parameters including time, temperature and medium on structural and optical properties of nanostructured materials, we have considered preformed Eu^{3+}-doped $La_2Zr_2O_7$ NPs which were initially synthesized by the MSS method at 650 °C. Thermal treatment and defect also play a very important role in order-disorder phase transition in case of $A_2B_2O_7$ type pyrochlore which is very important to understand from basic materials perspective [26,34,49].

2. Experimental

2.1. Chemicals

Sodium nitrate ($NaNO_3$, 99.0%), potassium nitrate (KNO_3, 99.0%), sodium chloride (NaCl, 99.5%), potassium chloride (KCl, 99.0%), and zirconium(IV) oxynitrate hydrate ($ZrO(NO_3)_2{\cdot}xH_2O$, 99.99%) were purchased from Sigma-Aldrich. Europium (III) nitrate hexahydrate ($Eu(NO_3)_3{\cdot}6H_2O$, 99.9%), lanthanum(III) nitrate hexahydrate ($La(NO_3)_3{\cdot}6H_2O$, 99.99%), and ammonium hydroxide (NH_4OH, 28%) were purchased from Alfa Aesar. All chemicals were used as received without further purification.

2.2. Synthesis

The preformed $La_2Zr_2O_7$:5%Eu^{3+} (LZOE-P) NPs were initially synthesized following a two-step procedure as specified by our previous publications [14,18,26,29,34,37]. Basically, the first step forms a single-source precursor of 95%$La(OH)_3$·5%$Eu(OH)_3$·$ZrO(OH)_2$·nH_2O via a coprecipitation process corresponding to the 5%Eu^{3+} doped $La_2Zr_2O_7$ NPs. In the second step, a kinetically modified molten salt method was used by first mixing the sodium and potassium nitrates with the formed single-source precursor in a ratio of 30:30:1 by grinding, then heated in a corundum crucible by a muffle furnace at 650°C for 6 h with ramp-up and -down rates of 5°C/min, and finally washed with DI water multiple times to remove the salts.

To investigate the effects of molten-salt processing on the structure, particle size, and optical properties of these preformed LZOE-P NPs, we mixed them with sodium and potassium nitrates or chlorides in a molar ratio of 1:30:30 and charged the new mixture under various processing times (3 h, 6 h, 12 h, and 24 h) and temperatures (i.e. 650 °C, 800 °C, 950 °C, and 1100 °C) with ramp-up and -down rates of 3°C/min. The obtained products after washed and purified with deionized water were denoted on the format of LZOE-t(the number of processing hours)-T(the number of processing temperature without the zeros)-molten-salt medium (shorted as N and C for the nitrate and chloride mixtures, respectively). For example, the preformed LZOE-P NPs after further molten-salt processing for 6 h at 1100 °C in the sodium and potassium nitrate molten-salt are named as LZOE-t6-T11-N. The schematic of the molten-salt processing of the preformed LZOE-P NPs is showed in Fig. 1.

2.3. Characterization

The LZOE NPs before and after further molten-salt processing were characterized using X-ray diffraction (XRD), Raman spectroscopy, scanning electron microscopy (SEM), photoluminescence spectroscopy (PL) and lifetime decay. XRD patterns were taken by Benchtop powder X-ray Rigaku-Miniflex diffractometer having a Cu $K\alpha_1$ radiation (λ = 0.15406 nm, 115 V, 50/60 Hz) with a scanning 2θ range of 20–90°, step size of 0.05° and rate of 1.12°/sec. Raman spectra were taken by a Senterra Bruker spectroscope (OPUS 7.5 Software) with a 785 nm laser and 50 mW at a resolution of 3–5 cm^{-1} and integration time of 10 s. SEM images were collected using a Carl Zeiss Sigma-VP field emission SEM. PL spectra were recorded using an Edinburgh Instrument FLS 980 fluorometer with a xenon lamp. Lifetime decay profiles were collected on the FLS 980 fluorometer by implementing a pulsed microsecond xenon lamp with a frequency from 1 to 100 Hz using time correlation with single photon counting method.

3. Results & discussion

For the simplicity of discussion, the molten-salt processing time and temperature studies were performed only in the sodium and potassium chloride medium.

3.1. Molten-salt processing time

3.1.1. XRD patterns

The purity of the LZOE NPs was confirmed by XRD. XRD patterns of the preformed LZOE NPs and those with further molten-salt process at 800 °C in mixed sodium and potassium chloride medium for different hours (Fig. 2a) show pure phase in line with the standard XRD pattern of LZO (JCPDS card No 71–2363).

To calculate the crystallite sizes of the preformed LZOE NPs and the LZOE NPs after further molten-salt processed with different times, the Debye-Scherrer formula was used:

$$D = \frac{k\lambda}{\beta \cos\theta} \quad (1)$$

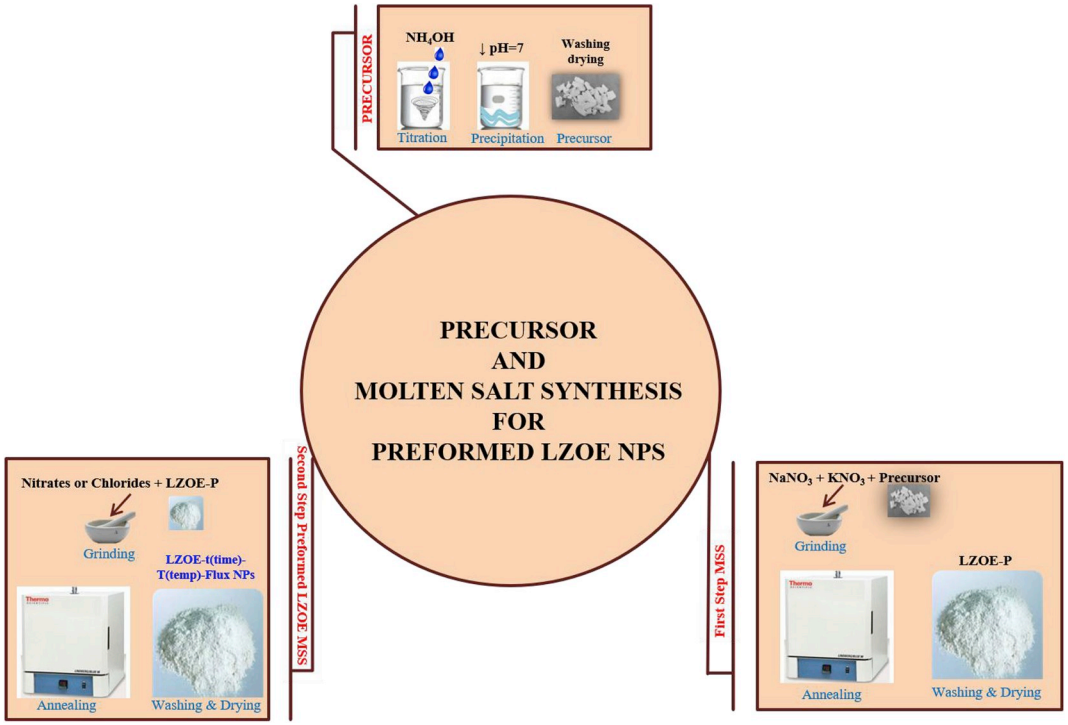

Fig. 1. Schematic of the molten-salt processing of the preformed LZOE-P NPs.

where D represents the crystallite size, K is a constant of the Scherrer formula with a value of 0.94 for cubic crystallites. λ is the X-ray wavelength with a value of 1.5406 Å, β is the full width half-maximum (FWHM) of the (222) peak of the NPs minus the FWHM fitting of the instrument, and θ is the angle of the corresponding Bragg reflection fitted in concord with the calculate FWHM of the (222) peak. The calculated crystallite size of the LZOE NPs (Table 1) clearly show that the particle size increases from 22 nm to 29 nm with increasing molten-salt processing time from 0 h to 24 h. The increase of crystallite size with the elongated molten salt processing time can be attributed to the increased diffusion of nanoparticles which causes continuous particle growth via Ostwald Ripening (OR). In most cases, the growth of nanoparticles takes place via two mechanisms: OR for highly soluble materials and oriented attachment (OA) for less soluble crystals. For OR, particle growth is due to the dissolution of smaller ones. In the OA process, particle growth occurs through merging smaller ones when exposed to high annealing temperature or long annealing time [50–52]. The OR explanation holds also feasible on annealing temperature for our LZOE NPs as shown in Table 2.

3.2. Raman spectra

Raman spectroscopy is a beneficial technique to study molecular vibration in a structure. When studying $A_2B_2O_7$ phase structures, it is one of the most sought out techniques to distinguish between disorder fluorite (DF) and ordered-pyrochlore (OP) structure. A DF structure with space group $Fm\bar{3}m$ only has one Raman active mode assigned to $4F_{2g}$ which is mainly attributed to random orientation of seven O^{2-} ions over eight anionic sites leading to high level of structural disordering. On the other hand, the OP structure with $Fd\bar{3}m$ space group has six Raman modes (A_{1g} + E_g + $4F_{2g}$) that occur in the range of 200 cm^{-1} to 1000 cm^{-1} [26,29,44]. The Raman spectra of the preformed LZOE NPs and those further molten-salt processed at 800 °C for various durations (Fig. 2b) displayed similar features consisting of pyrochlore

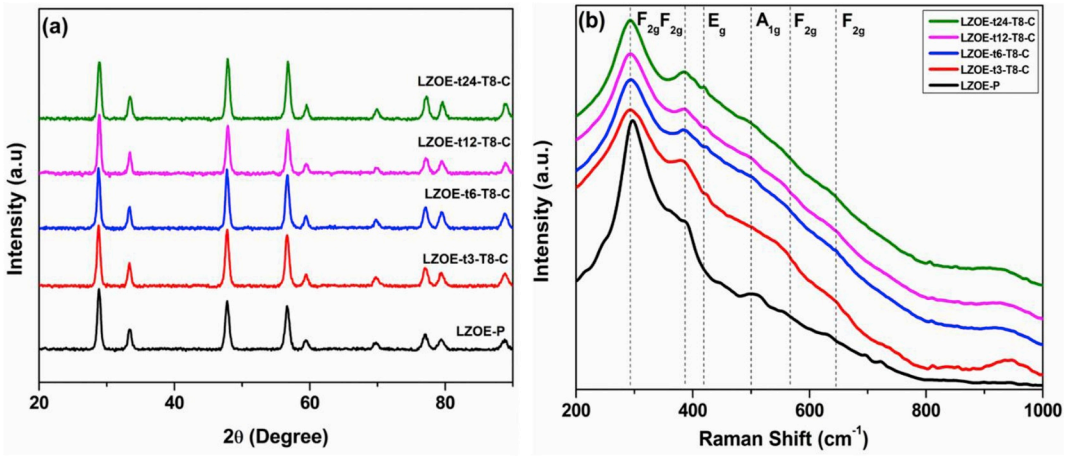

Fig. 2. (a) XRD patterns and (b) Raman spectra of the LZOE NPs preformed and after further molten salt processed at 800 °C in mixed sodium and potassium chloride medium with different durations.

Table 1
Changes of structural and optical parameters after the preformed LZOE NPs further molten salt processed at 800 °C in mixed sodium and potassium chloride medium with different durations.

	LZOE-P	LZOE-t3-T8-C	LZOE-t6-T8-C	LZOE-t12-T8-C	LZOE-t24-T8-C
2θ (°) of (222) peak	28.85	28.8	28.75	28.9	28.8
FWHM (β) of (222) peak	0.5742	0.5382	0.52397	0.50596	0.4874
Calculated crystallite size from XRD (nm)	22	24	25	27	29
Calculated lattice parameter (Å)	10.71	10.73	10.75	10.69	10.73
FWHM of Raman F_{2g} peak	326.43	503.609	534.46	535.99	519.34
Estimated particle size from SEM (nm)	32.4 ± 0.4	33.3 ± 0.4	37.4 ± 0.4	45.9 ± 0.8	47.5 ± 0.8
PL lifetime (ms)	1.76	1.77	1.65	1.84	1.95

Table 2
Changes in structural and optical parameters after molten-salt processing of the preformed LZOE NPs at different temperatures for 3 h in mixed sodium and potassium chloride molten-salt medium.

	LZOE-P	LZOE-t3-T8-C	LZOE-t3-T9-C	LZOE-t3-T11-C
2θ (°) of (222) peak	28.85	28.75	28.85	28.8
FWHM (β) of (222) peak	0.5742	0.5239	0.4454	0.43977
Calculated crystallite size (nm)	22	25	33	34
Calculated lattice parameter (Å)	10.71	10.75	10.71	10.73
FWHM of Raman F_{2g} peak	326.43	503.60	537.88	494.57
Estimated particle size from SEM (nm)	32.4 ± 0.4	33.3 ± 0.4	40.9 ± 0.5	49.7 ± 0.6
PL lifetime (ms)	1.76	1.77	2.16	1.99

structure. We observed the absence of well-resolved sextet (A_{1g} + E_g + $4F_{2g}$) of ideal pyrochlore structure and a broadening of the FWHM (Table 1) of the Raman bands with increasing molten-salt processing time compared to the preformed LZOE NPs. The increasing FWHM of the Raman F_{2g} band at ~300 cm^{-1} suggests increased anion disordering of the LZOE NPs after further molten-salt processed at 800 °C with increasing duration compared to the preformed ones [53]. These observations indicate that the LZOE NPs possess more and more disordered pyrochlore structure after elongated MSS processing time. The reason for this phenomenon is unclear at this moment as high-temperature exposure generally leads to cation/anion ordering. It is possible that 800 °C is only an intermediate processing temperature, which is high enough to motive random oscillation and motion of ions but is not sufficient to promote cation/anion ordering, or longer processing time is needed at this temperature. The latter point is plausible as we can see decreased FWHM as the processing duration is extended to 24 h which is an indication of increasing ordering (Fig. 2b and Table 1). The same observation and explanation hold true for the molten salt processing temperature for the same duration as shown in Fig. 5b and Table 2. Further studies are necessary to understand the underlying mechanism.

3.2.1. SEM

SEM was used to observe morphology and particle size changes of our preformed LZOE NPs after further molten-salt processing. SEM images (Fig. 3) and corresponding particle size (histogram insets and Table 1) show the LZOE NPs are spherical with a continuous progression of the average particle size from 32 nm to 48 nm before and after further molten-salt processing of the preformed LZOE NPs with different durations. Annealing solid-state crystalline materials to sufficiently high temperature enables Oswald ripening; i.e. larger grains grow bigger at the expense of smaller grains. The rate limiting factors are diffusion oriented. Hence, grain growth typically goes exponentially with temperature, only linearly with time at a given temperature like our case shown here [54].

3.2.2. PL: emission, excitation and lifetime spectra

Upon excited at the charge transfer band, the emission spectra of the LZOE NPs consist of strong bands of $^5D_0 \rightarrow {}^7F_1$ (592 nm), $^5D_0 \rightarrow {}^7F_2$ (612 nm), $^5D_0 \rightarrow {}^7F_3$ (653 nm) and $^5D_0 \rightarrow {}^7F_4$ (709 nm) (Fig. 4a). The orange emission at 592 nm belongs to the magnetic dipole $^5D_0 \rightarrow {}^7F_1$ transition of Eu^{3+} which hardly varies with the crystal field strength. The red emission at ~612 nm is ascribed to the electric dipole $^5D_0 \rightarrow {}^7F_2$ transition of Eu^{3+} which is very sensitive to the local environment around the Eu^{3+} and depends on the symmetry of the crystal field. The intensity ratio of $^5D_0 \rightarrow {}^7F_2$ to $^5D_0 \rightarrow {}^7F_1$ known as asymmetry ratio provides structural information about the local symmetry around Eu^{3+} ions in the LZOE NPs. The fact that $^5D_0 \rightarrow {}^7F_1$ line at 612 nm (ED) is very strong in comparison to $^5D_0 \rightarrow {}^7F_1$ line at 592 nm (MD) indicates that Eu^{3+} occupy relatively asymmetric environment with no inversion symmetry. Moreover, the large stark splitting of the Eu^{3+} emission spectra also support the hypothesis that Eu^{3+} ions are localized at low symmetric site. In LZO, La site is oriented in distorted scalenohedral whereas Zr is oriented in perfect octahedra [26]. The emission spectral patterns here reflect the fact that large fraction of Eu^{3+} ions are localized in LaO_8 site. The excitation spectra of the LZOE NPs (Fig. 4c) consist of a broad band in the range of 250–360 nm and several lines in the range of 360–420 nm. The broad excitation band can be attributed to the charge transfer (CT) transition from $O^{2-} \rightarrow Eu^{3+}$ ions. The sharp lines in the range of 360–420 nm are associated with the inter-configurational f-f transitions of Eu^{3+} ions. The relative intense peak at 393 nm is ascribed to $^7F_0 \rightarrow {}^5L_6$.

Moreover, the emission and excitation spectral profile of the preformed LZOE NPs does not change much after different molten-salt processing durations unlike the intensity (Fig. 4a and c). The variation of emission intensity as a function of the molten-salt processing time clearly show that the preformed LZOE NPs have maximum emission intensity which reduces drastically once molten-salt processed at 800 °C in mixed sodium and potassium chloride medium for different time durations (Fig. 4b). This is attributed to light scattering by particle aggregates which achieve grain growth once exposed to extended molten-salt processing time. The resulted agglomerate causes scattering of both excited and emitted light leading to reduction in emission intensity [55]. Another reason is thermal quenching by non-radiative relaxation. The typical nonradiative relaxation mechanisms of Eu^{3+} emission include: (i) multiphoton relaxation, (ii) temperature dependent energy transfer, and (iii) crossover from the $4f$ [6] electronic configuration of Eu^{3+} ion to a charge transfer state [56]. The reduction of surface defect after post-synthesis thermal treatment is a competing factor and should have led to enhancement of emission intensity because surface defects are a source of non-radiative pathway [25]. However, the effect of light scattering is more predominate than non-

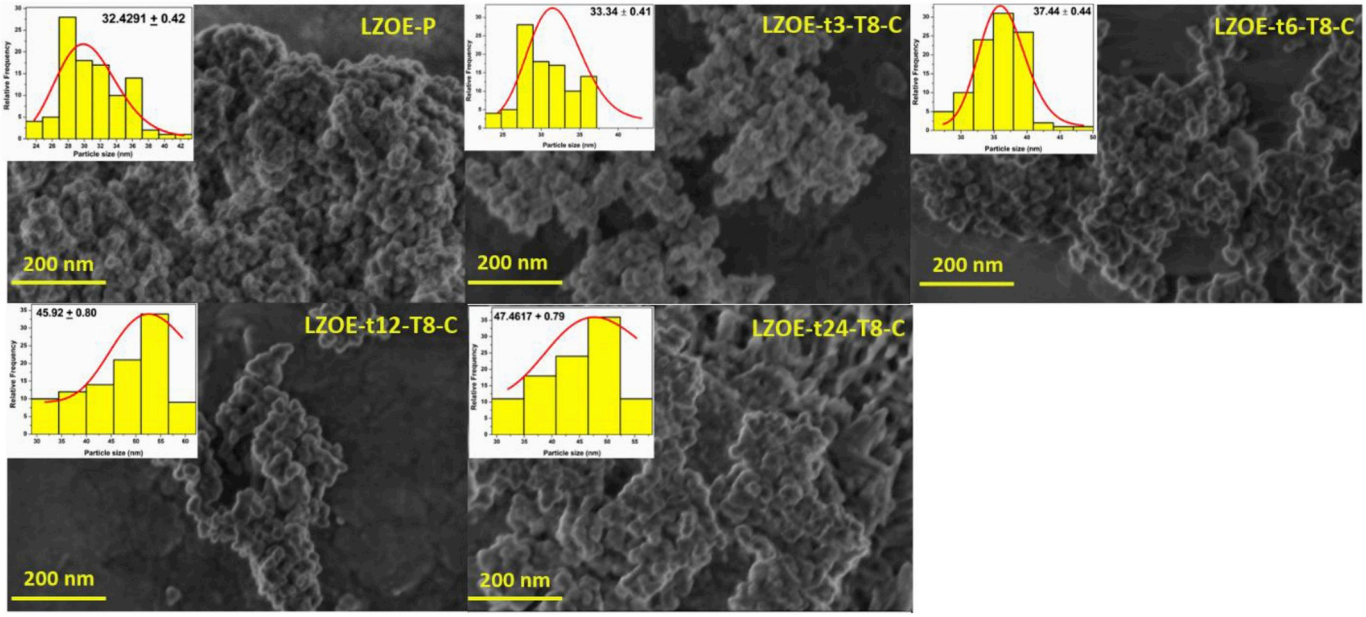

Fig. 3. SEM images of the LZOE NPs before and after molten-salt processed at 800 °C in mixed sodium and potassium chloride medium with different durations. The insets show the histograms of the particle size obtained from the ImageJ software.

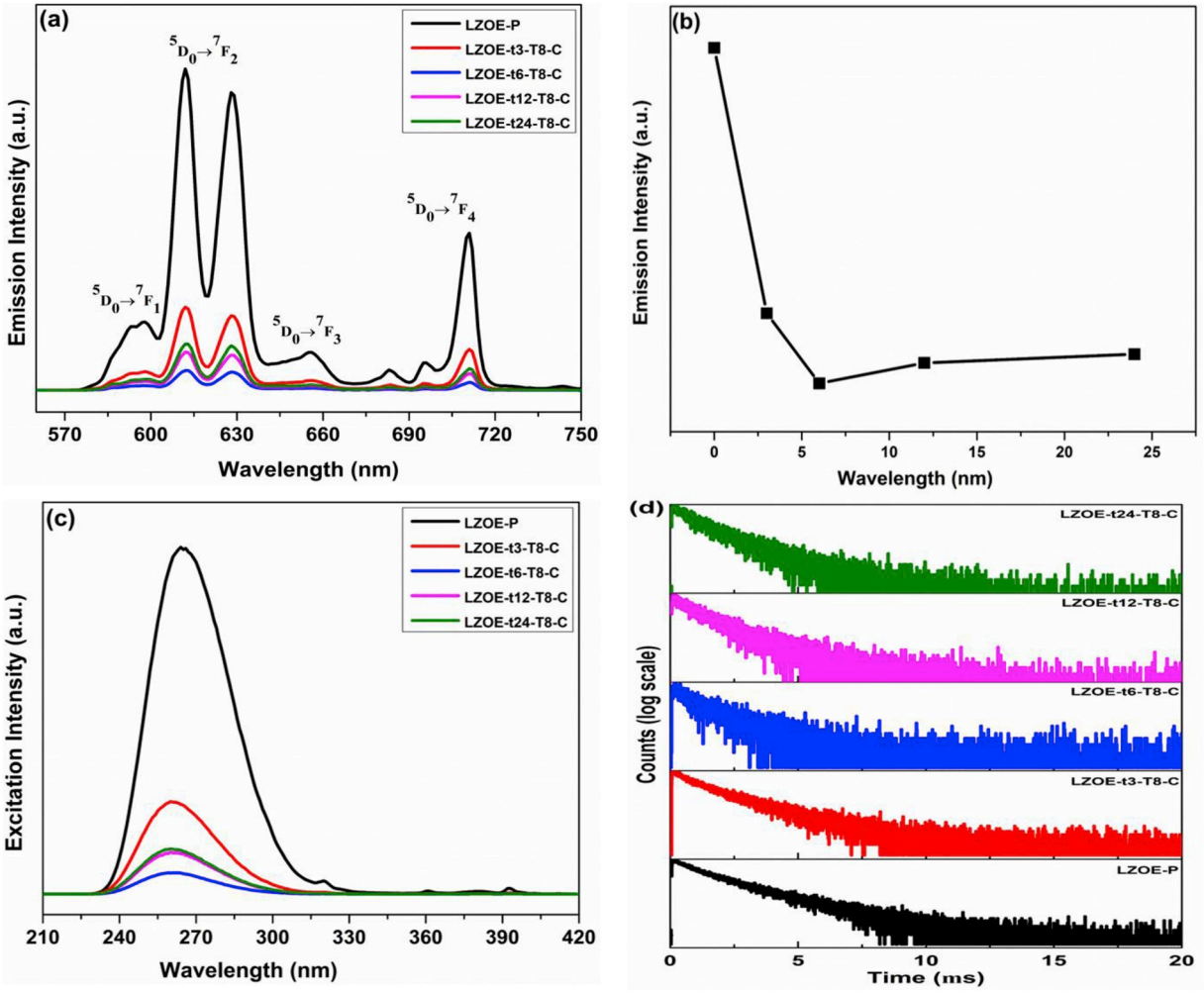

Fig. 4. (a) Emission spectra (λ_{ex} = 260 nm), (b) variation of emission intensity as a function of processing time, (c) excitation spectra (λ_{em} = 612 nm), and (d) lifetime decay profiles of the LZOE NPs before and after molten-salt processed at 800 °C in sodium and potassium chloride medium with different durations.

radiative relaxation by surface defects.

Among the molten-salt processed LZOE samples for duration of 3 h–24 h, the 3 h sample has maximum intensity which can be attributed to its high-quality characteristics in terms of decreased defects, increased crystallinity and minimum agglomeration [18]. These contributing factors are proposed based on our previous work on thermally treating pyrochlore rare earth hafnate and zirconate nanoparticles with BET surface area measurement and positron annihilation lifetime spectroscopy, i.e. surface area decreases with increasing annealing time/temperature [25,26]. More specifically, surface defects of our LZOE NPs are proportional to their surface area: the larger the surface area of the LZOE NPs, the more Eu^{3+} ions localized near their surface. As a general rule, surface defects are known to provide additional pathways for non-radiative transitions and quench luminescence [57]. At the same time, with increasing processing time/temperature, the crystallinity and agglomeration of the particles increase. Particles form hard agglomerates which scatter excitation/emission light and decrease luminescence. Our previous work on $La_2Hf_2O_7$:Eu^{3+} NPs also suggested that 3 h processing time is the best duration to optimize quantum yield and photo/radioluminescence output [18].

There is slight emission intensity enhancement beyond 6 h which is due to the dominating effect of surface defects while surface defects decrease at longer processing duration over particle agglomeration.

To get an idea about the nature of the dopant Eu^{3+} occupancy in the LZO lattice sites, PL decay time (lifetime) studies were conducted. The decay curves corresponding to the $^5D_0$ level of Eu^{3+} ions of the LZOE NPs (Fig. 4d) depict monoexponential profiles. This suggested that the Eu^{3+} ions are homogeneously distributed in the LZOE NPs. Earlier emission spectroscopic results revealed that large fraction of Eu^{3+} ions are stabilized at LaO_8 site which is in line with the monoexponential decay behavior. Moreover, there is not much difference of the corresponding lifetime values for the preformed LZOE NPs and the molten salt processed NPs for 3 h (Table 1). The lifetime value initially decreases from the 3 h processed sample to the 6 h processed sample, and then keep increasing further up to the 24 h processed sample. The initial decrease of the lifetime value is due to the agglomeration effect dominating surface defect whereas the opposite phenomenon prevails at elongating molten-salt processing duration [18].

3.3. Molten-salt processing temperature

3.3.1. XRD patterns

The XRD patterns (Fig. 5a) clearly show the formation of single-phase products without any impurity in accordance with JCPDS pattern 71–2363. The sharp diffraction peaks reflect high crystallinity of the LZOE NPs. The crystalline size increases from 22 nm to 34 nm as the molten-salt processing temperature increases from 650 °C to 1100 °C. This is attributed to Ostwald ripening again [58], i.e. larger grains grow bigger at the expense of smaller grains demonstrating that is a function of the surface area to volume ratio (S/V). Also, the change of crystalline size of the LZOE NPs induced by the molten-salt processing temperature is larger than that caused by molten-salt processing time.

3.3.2. Raman spectra

The Raman spectra (Fig. 5b) suggests that the preformed LZOE NPs are stabilized in the pyrochlore structure after thermal treatment at different temperatures for 3 h in mixed sodium and potassium chloride molten-salt medium. Again, the absence of well-resolved sextet characteristic of ideal pyrochlore and the broader peaks than usual indicate that the processed LZOE NPs process disordered pyrochlore structure. Moreover, the peaks become narrower with increasing molten-salt processing temperature from 800 to 1100 °C which suggests the extent of structural ordering increases (Table 2) [29]. Therefore, both XRD and Raman data (Fig. 5a-b) indicate that, as the preformed LZOE NPs are exposed to increasing molten-salt processing temperature up to 900 °C, Ostwald ripening induced the particle growth of the LZOE NPs and the crystal structure becomes more and more disordered, respectively. Beyond that, the structure starts regaining structural orderings at 1100 °C as can be seen from the reduction of the FWHM of Raman bands compared to those from the NPs processed at 900 °C.

3.3.3. SEM images

SEM images (Fig. 6) clearly show that the preformed LZOE particles form spheres in nanodomain but start to aggregate as they are exposed to increasing molten-salt processing temperature. As post-synthesis molten-salt processing temperature increases, the particle size grows from 33 nm to 50 nm (insets of Fig. 6 and Table 2). In other words, the small NPs self-assemble into spheres of large aggregates. These spheres start forming clusters around them and finally rearrange themselves into large sized NPs [59]. Yang et al. explained how nanomaterials tend to assemble in different forms by mechanical properties being organized by surface and strength of the nanoparticle adhesion [10]. The trend of the estimated average particle size of the LZOE NPs through the histograms obtained by the ImageJ software on the SEM images is in line with the calculated crystallite size based on XRD data.

3.3.4. PL: emission, excitation and lifetime spectra

There is monotonic gradual decrease of the PL emission intensity as a function of the molten-salt processing temperature (Fig. 7a). This is attributed to high temperature induced particle agglomeration and the

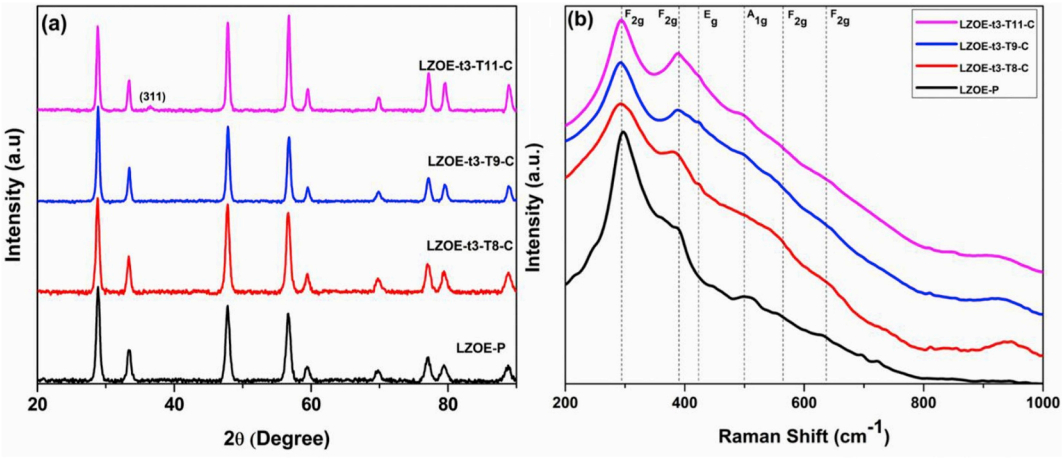

Fig. 5. (a) XRD patterns and (b) Raman spectra of the LZOE NPs before and after further molten-salt processed at different temperatures for 3 h in mixed sodium and potassium chloride molten-salt medium.

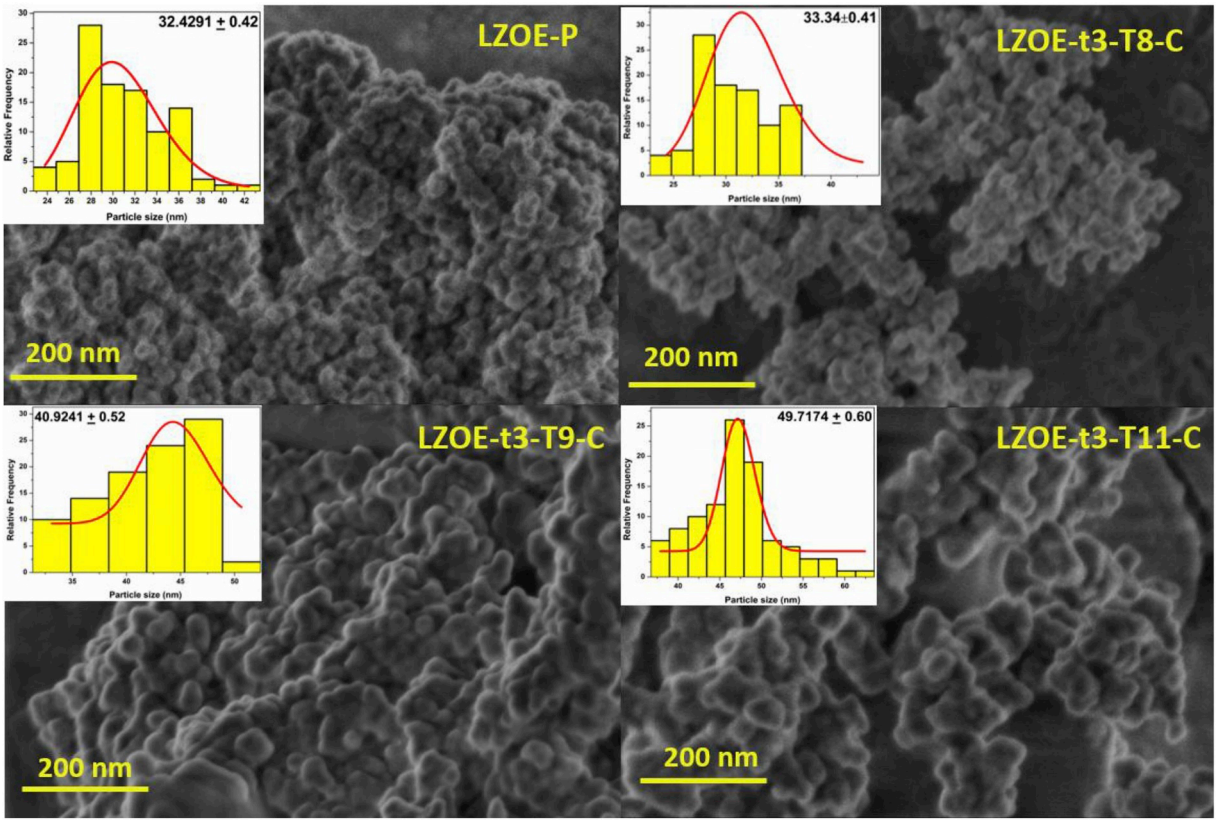

Fig. 6. SEM images of the preformed LZOE NPs before and after molten-salt processing at different temperatures for 3 h in mixed sodium and potassium chloride molten-salt medium. The insets show the histograms of the average particle size estimated using the ImageJ software.

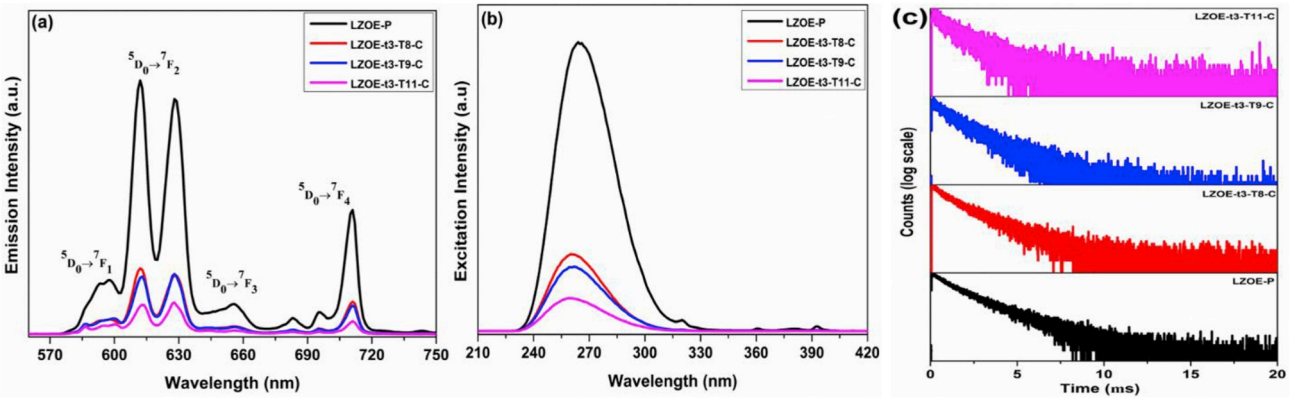

Fig. 7. (a) Emission spectra (λ_{ex} = 260 nm), (b) excitation spectra (λ_{em} = 612 nm), and (c) lifetime decay profiles (λ_{ex} = 260 nm and (λ_{em} = 612 nm) of the LZOE NPs before and after molten-salt processed at different temperatures for 3 h in mixed sodium and potassium chloride molten-salt medium.

resulted agglomerate causes scattering of both excited and emitted light leading to reduction in emission intensity [55]. Another reason is thermal quenching by non-radiative relaxation. Moreover, high temperature annealing is reported to create several thermal defects such as cation vacancies, interstitials, etc. [60], which are expected to reduce the emission intensity by providing nonradiative pathways. Overall, the effect of light scattering is more predominate than nonradiative relaxation by surface defects.

It was also observed that the energy of CT band increases (shifts towards shorter wavelengths) with increasing molten-salt processing temperature (Fig. 7b). This can be explained by the expansion of the lattice leading to the increased average distance between Eu^{3+} and surrounding anions, thus making it difficult for the electron transfer from oxygen to europium. The PL excitation and emission spectra conclusively confirm the enhancement of the O→Eu charge transfer energy and thermal quenching of emission intensity with post-synthesis thermal treatment at high temperature of the LZOE NPs. Due to the large size of our LZOE NPs, this energy change of CT band cannot be attributed to quantum confinement effect [61].

The preformed LZOE NPs after molten-salt processing at different temperatures (Fig. 7c) show monoexponential decay profiles corresponding to the $^5D_0$ level of Eu^{3+} ions. The lifetime value of the LZOE NPs (Table 2) increases progressively with the molten-salt processing temperature up to 950 °C and then slightly decreases at 1100 °C. This is due to the surface area reduction at higher processing temperature and the increase of particle size. Surface defects on NPs are related to their surface area. Larger the surface area, more Eu^{3+} ions are located near the surface, and more surface defects which can quench the fluorescence. The enhancement in excited state lifetime up to 950 °C can be ascribed to the decrease of surface area/surface defect ratio [62,63].

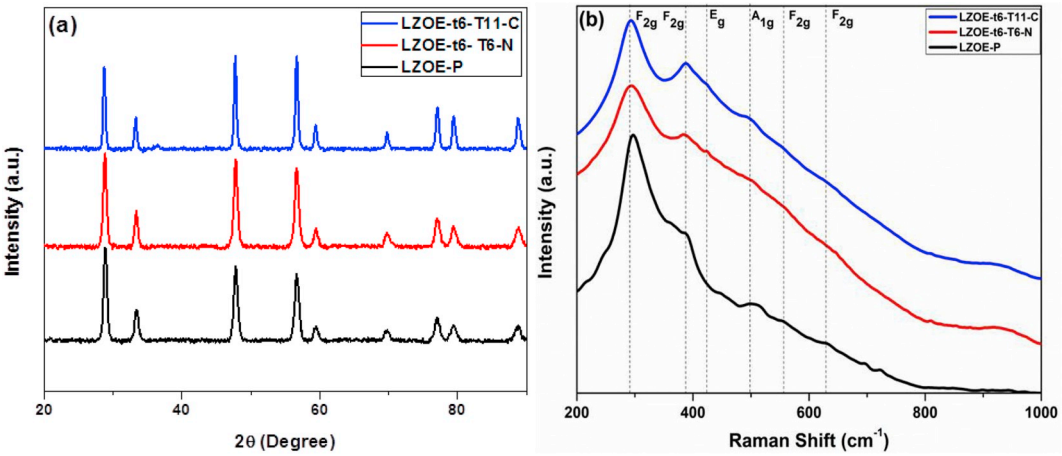

Fig. 8. (a) XRD patterns and (b) Raman spectra of the LZOE NPs before and after processed in the $NaNO_3$–KNO_3 and NaCl–KCl molten-salt media for 6 h at 650 °C and 1100 °C, respectively.

Table 3
Changes in structural and optical parameters of the preformed LZOE NPs after further molten-salt processing at 650 °C and 1100 °C for 6 h in mixed sodium and potassium nitrate and chloride media.

	LZOE-P	LZOE-t6-T6-N	LZOE-t6-T11-C
2θ (°) of (222) peak	28.85	28.8	28.7
FWHM (β) of (222) peak	0.5742	0.5382	0.39227
Calculated crystallite size (nm)	22	24	42
Calculated lattice parameter (Å)	10.71	10.73	10.76
FWHM of Raman F_{2g} peak	326.43	534.46	505.54
Estimated particle size from SEM (nm)	32.4 ± 0.4	42.3 ± 0.6	59.3 ± 0.9
PL lifetime (ms)	1.76	1.65	1.99

Beyond 950 °C, the NPs tend to agglomerate to such an extent which overpowers the effect of surface area and causes scattering of the emitted light and decreases the lifetime value. Therefore, the slight reduction in lifetime value beyond certain molten-salt processing temperature is attributed to increased crystallite size and agglomerates, which tend to scatter light and lead to decrease of emission intensity [64].

3.4. Molten-salt processing medium

3.4.1. XRD patterns

Here we also further processed the preformed LZOE NPs in two different molten-salt media, i.e. $NaNO_3$–KNO_3 (at 650 °C for 3 h) and NaCl–KCl (at 1100 °C for 3 h) with equimolar pseudo-eutectic melting points of 228 and 657 °C, respectively [65,66]. The XRD patterns of LZOE (Fig. 8a) are perfectly coincided with characteristic diffraction lines of the $La_2Zr_2O_7$ in accordance with JCPDS pattern 71–2363 except of intensity, and no characteristic peaks of other impurities are observed. The calculated cell parameters and crystallite sizes of the LZOE NPs before and after processed in different molten-salt media are tabulated in Table 3.

3.4.2. Raman spectra

The Raman spectra (Fig. 8b) confirmed the pyrochlore phase of the preformed LZOE NPs before and after further processed in the two molten-salt media. The absence of well-resolved sextet of ideal pyrochlore structure and broad peaks suggest the disordered pyrochlore nature of these LZOE NPs. The LZOE-C sample shows higher ordering of the oxygens in ordered pyrochlore phase with increased intensity and narrowed bands in comparison with the LZOE-N samples (Table 3). This phenomenon is attributed to increased ordering of LZOE lattice at high temperature in case of chloride flux. However, the preformed LZOE NPs still have the most ordered anion sublattice.

3.4.3. Scanning electron microscope

The larger particle size of the LZOE NPs processed in the chloride medium compared to the nitrate medium is supported by the SEM images (Fig. 9). Particle formation in MSS is governed by nucleation and crystal growth process and their rate ratio determine the particle size and shape [65]. Higher the rate of nucleation, larger the particle size, and more closer shape to crystal structure. On the other hand, when the rate of crystal growth exceeds nucleation, uniform particles

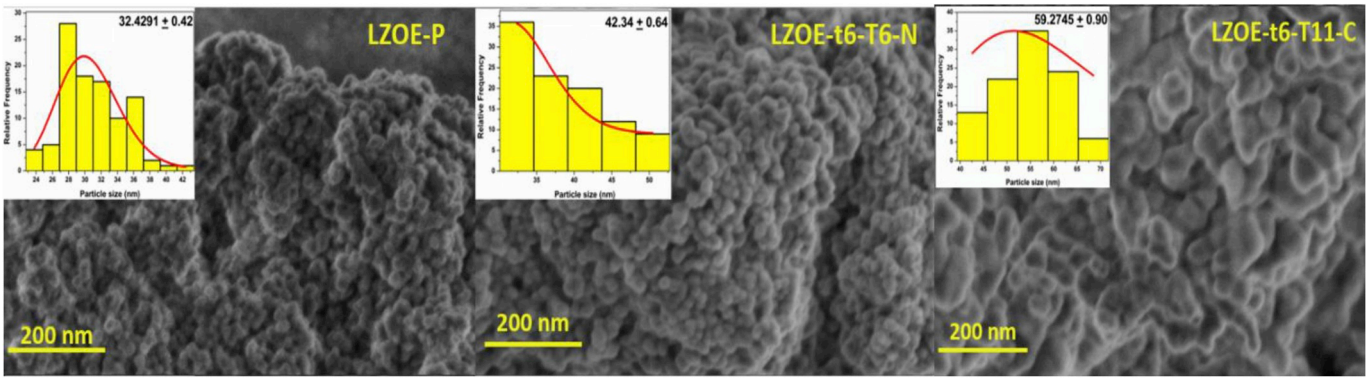

Fig. 9. SEM images of the LZOE NPs before and after processed in the mixed sodium and potassium nitrate and chloride media for 6 h at 650 °C and 1100 °C, respectively. The insets show the histograms of the average particle size calculated using the ImageJ software.

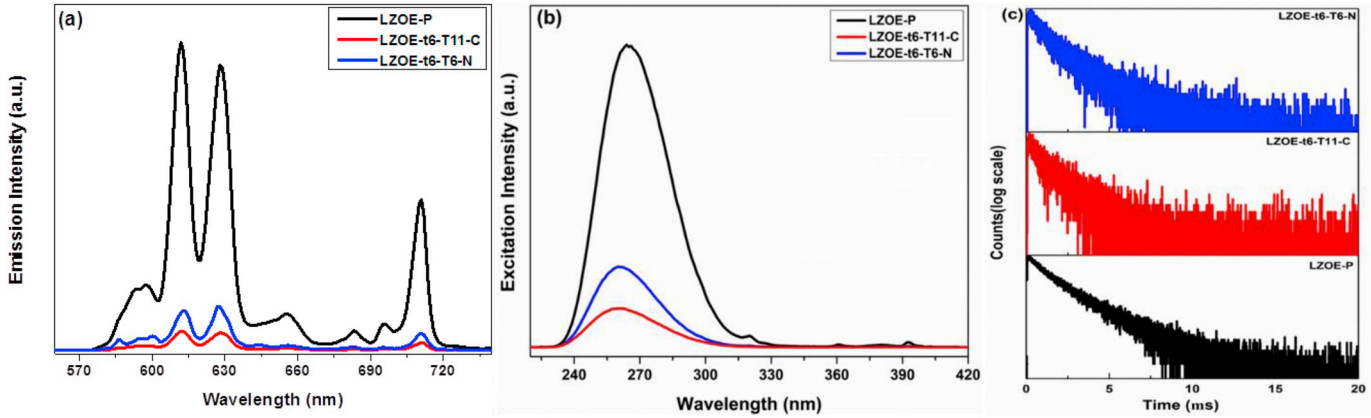

Fig. 10. (a) Emission spectra (λ_{ex} = 260 nm), (b) excitation spectra (λ_{em} = 612 nm) (c) Lifetime decay profiles (λ_{ex} = 260 nm and λ_{em} = 612 nm) of the LZOE NPs before and after processed in the mixed sodium and potassium nitrate and chloride media for 6 h at 650 °C and 1100 °C, respectively.

are formed. The mean particle size of the obtained sample prepared by KNO_3–$NaNO_3$ fluxes at 6 h/650 °C is about 42 nm and that of as-synthesized sample in term of KCl–NaCl fluxes at 6 h/1100 °C is approximately 59 nm, implying that the kind of molten-salt flux has great effect on the particle size of the obtained samples. The reason for this phenomenon may be that higher molten-salt processing temperature is in favor of forming lager particle size, since the processing temperature of the LZOE NPs in the $NaNO_3$–KNO_3 flux is lower than that of the LZOE NPs in the presence of NaCl–KCl flux [67].

3.4.4. PL: emission, excitation and lifetime spectra

Emission (Fig. 10a) and excitation spectra (Fig. 10b) of the LZOE NPs after processed in the two molten-salt media show different intensities. The LZOE NPs treated in the nitrate medium have higher emission/excitation intensity than the counterpart treated in the chloride medium while both samples have lower intensity compared to the preformed LZOE NPs. This observation is attributed to light scattering by agglomerates of the LZOE NPs, especially the larger ones treated in the chloride medium. The lifetime values (Table 3) obtained from the lifetime decay profiles (Fig. 10c) show that it is larger for the NPs treated in the chloride medium than the sample treated in the nitrate medium. This is attributed to large defect density for the latter compared to the former which has more predominating effect compared to agglomeration.

4. Conclusion

This work highlighted the roles of post-synthesis molten-salt processing time, temperature and medium type on the preformed molten-salt synthesized $La_2Zr_2O_7$:Eu^{3+} nanoparticles. The LZOE NPs under these investigations were carried out by X-ray diffraction, Raman spectroscopy, scanning electron microscopy, and time resolved photoluminescence to decipher their size, shape, structure and optical property changes. Raman spectroscopy confirms the stabilization of pyrochlore structure of the LZOE NPs with observed thermally induced disordering. It was observed that longer processing time and higher processing temperature lead to enhanced crystal growth and increased lattice disordering. Moreover, no much change of particle shape of the NPs was observed but the nanoparticles tend to aggregate at longer processing time and higher processing temperature. Molten-salt processing in chloride medium increases crystalline quality and uniform grain growth owing to their higher melting point of chloride flux. Luminescence decay investigations showed a decrease in lifetime value as the molten-salt processing time and temperature were raised due to decrease of defects under enhanced thermal condition. This work highlights the importance of post-synthesis thermal treatment conditions on tuning the size, structure and property of preformed nanoparticles.

Notes

The authors state no contending financial interest.

Acknowledgement

The authors thank the financial support by the National Science Foundation under CHE (award #1710160) and the IIT startup funds. SKG thanks the United States-India Education Foundation (USIEF, India) and the Institute of International Education (IIE, USA) for his Fulbright Nehru Postdoctoral Fellowship (Award# 2268/FNPDR/2017).

References

[1] K. Zhang, H. Gao, R. Deng, J. Li, Emerging applications of nanotechnology for controlling cell-surface receptor clustering, Angew. Chem. Int. Ed. 58 (15) (2019) 4790–4799.
[2] R. Paul, F. Du, L. Dai, Y. Ding, Z.L. Wang, F. Wei, A. Roy, 3D heteroatom-doped carbon nanomaterials as multifunctional metal-free catalysts for integrated energy devices, Adv. Mater. 31 (13) (2019) 1805598.
[3] H. Xiang, Y. Chen, Energy-converting nanomedicine, Small 15 (13) (2019) 1805339.
[4] U. Manzoor, F. Tuz Zahra, S. Rafique, M.T. Moin, M. Mujahid, Effect of synthesis temperature, nucleation time, and postsynthesis heat treatment of ZnO nanoparticles and its sensing properties, J. Nanomater. 2015 (2015) 6.
[5] A.G. Muradova, M.P. Zaytseva, A.I. Sharapaev, E.V. Yurtov, Influence of temperature and synthesis time on shape and size distribution of Fe_3O_4 nanoparticles obtained by ageing method, Colloid. Surf. Physicochem. Eng. Asp. 509 (2016) 229–234.
[6] H.S. Wasly, M.S.A. El-Sadek, M. Henini, Influence of reaction time and synthesis temperature on the physical properties of ZnO nanoparticles synthesized by the hydrothermal method, Appl. Phys. A 124 (1) (2018) 76.
[7] B.D. Ngom, T. Mpahane, E. Manikandan, M. Maaza, ZnO nano-discs by lyophilization process: size effects on their intrinsic luminescence, J. Alloy. Comp. 656 (2016) 758–763.
[8] M.-A. Einarsrud, T. Grande, 1D oxide nanostructures from chemical solutions, Chem. Soc. Rev. 43 (2014) 2187–2199.
[9] X. Liu, N. Fechler, M. Antonietti, Salt melt synthesis of ceramics, semiconductors and carbon nanostructures, Chem. Soc. Rev. 42 (2013) 8237–8265.
[10] E.K. Akdogan, R.E. Brennan, M. Allahverdi, A. Safari, Effects of molten salt synthesis (MSS) parameters on the morphology of $Sr_3Ti_2O_7$ and $SrTiO_3$ seed crystals, J. Electroceram. 16 (2) (2006) 159–165.
[11] J. Chen, A single-source molten salt synthesis of rod-shaped $Na_2Ti_6O_{13}$ crystals, Ceram. Int. 41 (7) (2015) 9018–9023.
[12] B.L. Cushing, V.L. Kolesnichenko, C.J. O'Connor, Recent advances in the liquid-phase syntheses of inorganic nanoparticles, Chem. Rev. 104 (9) (2004) 3893–3946.
[13] Z. Li, X. Zhang, J. Hou, K. Zhou, Molten salt synthesis of anisometric $Sr_3Ti_2O_7$ particles, J. Cryst. Growth 305 (1) (2007) 265–270.
[14] Y. Mao, X. Guo, J.Y. Huang, K.L. Wang, J.P. Chang, Luminescent nanocrystals with $A_2B_2O_7$ composition synthesized by a kinetically modified molten salt method, J. Phys. Chem. C 113 (4) (2009) 1204–1208.
[15] Y. Mao, T.-J. Park, F. Zhang, H. Zhou, S.S. Wong, Environmentally friendly methodologies of nanostructure synthesis, Small 3 (7) (2007) 1122–1139.
[16] H. Xie, J. Chen, B. Lei, L. Zhou, A Single-Source Molten Salt Synthesis of Uniform Octahedral $Na_2Ti_3O_7$ Particels Composed of Nanorods, (2018) *arXiv preprint arXiv:1803.02951*.

[17] J.P. Zuniga, M. Abdou, S.K. Gupta, Y. Mao, Molten-salt synthesis of complex metal oxide nanoparticles, JoVE (J. Vis. Exp.) 140 (2018) e58482.

[18] J.P. Zuniga, S.K. Gupta, M. Abdou, Y. Mao, Effect of molten salt synthesis processing duration on the photo-and radioluminescence of UV-, visible-, and X-ray-excitable $La_2Hf_2O_7:Eu^{3+}$ nanoparticles, ACS Omega 3 (7) (2018) 7757–7770.

[19] A.M. Beyene, C. Baek, W.K. Jung, P. Ragupathy, D.K. Kim, Understanding the role of oxygen ion (O^{2-}) activity in 1-D crystal growth of rutile TiO_2 in molten salts, CrystEngComm 20 (2018) 487–495.

[20] J. Lim, D. Park, S.S. Jeon, C.-W. Roh, J. Choi, D. Yoon, M. Park, H. Jung, H. Lee, Ultrathin IrO_2 nanoneedles for electrochemical water oxidation, Adv. Funct. Mater. 28 (2018) 1704796.

[21] M.V. Reddy, T.T. Linh, D.T. Hien, B.V.R. Chowdari, SnO_2 based materials and their energy storage studies, ACS Sustain. Chem. Eng. 4 (2016) 6268–6276.

[22] H.L. Thi N'Goc, L.D.N. Mouafo, C. Etrillard, A. Torres-Pardo, J.-F. Dayen, S. Rano, G. Rousse, C. Laberty-Robert, J.G. Calbet, M. Drillon, C. Sanchez, B. Doudin, D. Portehault, Surface-driven magnetotransport in perovskite nanocrystals, Adv. Mater. 29 (2017) 1604745.

[23] Y. Mao, T.J. Park, F. Zhang, H. Zhou, S.S. Wong, Environmentally friendly methodologies of nanostructure synthesis, Small 3 (2007) 1122–1139.

[24] Y. Mao, T. Tran, X. Guo, J.Y. Huang, C.K. Shih, K.L. Wang, J.P. Chang, Luminescence of nanocrystalline erbium-doped yttria, Adv. Funct. Mater. 19 (5) (2009) 748–754.

[25] S.K. Gupta, K. Sudarshan, P. Ghosh, A. Srivastava, S. Bevara, P. Pujari, R. Kadam, Role of various defects in the photoluminescence characteristics of nanocrystalline $Nd_2Zr_2O_7$: an investigation through spectroscopic and DFT calculations, J. Mater. Chem. C 4 (22) (2016) 4988–5000.

[26] S.K. Gupta, J.P. Zuniga, M. Abdou, Y. Mao, Thermal annealing effects on $La_2Hf_2O_7:Eu^{3+}$ nanoparticles: a curious case study of structural evolution and site-specific photo-and radio-luminescence, Inorg. Chem. Front. 5 (10) (2018) 2508–2521.

[27] N. Pathak, P.S. Ghosh, S.K. Gupta, S. Mukherjee, R.M. Kadam, A. Arya, An insight into the various defects-induced emission in $MgAl_2O_4$ and their tunability with phase behavior: combined experimental and theoretical approach, J. Phys. Chem. C 120 (7) (2016) 4016–4031.

[28] N. Pathak, S.K. Gupta, C.L. Prajapat, S.K. Sharma, P.S. Ghosh, B. Kanrar, P.K. Pujari, R.M. Kadam, Defect induced ferromagnetism in MgO and its exceptional enhancement upon thermal annealing: a case of transformation of various defect states, Phys. Chem. Chem. Phys. 19 (19) (2017) 11975–11989.

[29] S. Gupta, J. Zuniga, P. Ghosh, M. Abdou, Y. Mao, Correlating structure and luminescence properties of undoped and $La_2Hf_2O_7:Eu^{3+}$ NPs prepared with different coprecipitating pH values through experimental and theoretical studies, Inorg. Chem. 57 (2018) 11815–11830.

[30] S.K. Gupta, K. Sudarshan, P.S. Ghosh, K. Sanyal, A.P. Srivastava, A. Arya, P.K. Pujari, R.M. Kadam, Luminescence of undoped and Eu^{3+} doped nanocrystalline $SrWO_4$ scheelite: time resolved fluorescence complimented by DFT and positron annihilation spectroscopic studies, RSC Adv. 6 (5) (2016) 3792–3805.

[31] V. Valtchev, G. Majano, S. Mintova, J. Pérez-Ramírez, Tailored crystalline microporous materials by post-synthesis modification, Chem. Soc. Rev. 42 (1) (2013) 263–290.

[32] M.S. Morey, S. O'Brien, S. Schwarz, G.D. Stucky, Hydrothermal and postsynthesis surface modification of cubic, MCM-48, and ultralarge pore SBA-15 mesoporous silica with titanium, Chem. Mater. 12 (4) (2000) 898–911.

[33] W.J. Mir, Y. Mahor, A. Lohar, M. Jagadeeswararao, S. Das, S. Mahamuni, A. Nag, Postsynthesis doping of Mn and Yb into $CsPbX_3$ (X = Cl, Br, or I) perovskite nanocrystals for downconversion emission, Chem. Mater. 30 (22) (2018) 8170–8178.

[34] M. Abdou, S.K. Gupta, J.P. Zuniga, Y. Mao, On structure and phase transformation of uranium doped $La_2Hf_2O_7$ nanoparticles as an efficient nuclear waste host, Mater. Chem. Front. 2 (12) (2018) 2201–2211.

[35] S.K. Gupta, C. Reghukumar, K. Sudarshan, P. Ghosh, N. Pathak, R. Kadam, Orange-red emitting $Gd_2Zr_2O_7:Sm^{3+}$: structure-property correlation, optical properties and defect spectroscopy, J. Phys. Chem. Solids 116 (2018) 360–366.

[36] K.K. Rao, T. Banu, M. Vithal, G. Swamy, K.R. Kumar, Preparation and characterization of bulk and nano particles of $La_2Zr_2O_7$ and $Nd_2Zr_2O_7$ by sol–gel method, Mater. Lett. 54 (2–3) (2002) 205–210.

[37] J.P. Zuniga, S.K. Gupta, M. Pokhrel, Y. Mao, Exploring the optical properties of $La_2Hf_2O_7:Pr^{3+}$ nanoparticles under UV and X-ray excitation for potential lighting and scintillating applications, New J. Chem. 42 (12) (2018) 9381–9392.

[38] S. Ekambaram, K.C. Patil, M. Maaza, Synthesis of lamp phosphors: facile combustion approach, J. Alloy. Comp. 393 (1) (2005) 81–92.

[39] S. Ekambaram, M. Maaza, Combustion synthesis and luminescent properties of Eu^{3+}-activated cheap red phosphors, J. Alloy. Comp. 395 (1) (2005) 132–134.

[40] S.T. Aruna, A.S. Mukasyan, Combustion synthesis and nanomaterials, Curr. Opin. Solid State Mater. Sci. 12 (3) (2008) 44–50.

[41] K.V. Manukyan, S.V. Aydinyan, K.G. Kirakosyan, S.L. Kharatyan, G. Blugan, U. Müller, J. Kuebler, Molten salt-assisted combustion synthesis and characterization of $MoSi_2$ and $MoSi_2$-Si_3N_4 composite powders, Chem. Eng. J. 143 (1) (2008) 331–336.

[42] G. Huang, C. Wang, S. Xu, S. Zong, J. Lu, Z. Wang, C. Lu, Y. Cui, Postsynthetic doping of $MnCl_2$ molecules into preformed CsPbBr3 perovskite nanocrystals via a halide exchange-driven cation exchange, Adv. Mater. 29 (29) (2017) 1700095.

[43] N.M. Cepeda-Sánchez, J.A. Díaz-Guillén, M. Maczka, U. Amador, A.F. Fuentes, Cations size mismatch versus bonding characteristics: synthesis, structure and oxygen ion conducting properties of pyrochlore-type lanthanide hafnates, J. Mater. Sci. 53 (19) (2018) 13513–13529.

[44] S.K. Gupta, M. Abdou, J.P. Zuniga, P.S. Ghosh, E. Molina, B. Xu, M. Chipara, Y. Mao, Roles of oxygen vacancies and pH induced size changes on photo- and radioluminescence of undoped and Eu^{3+}-doped $La_2Zr_2O_7$ nanoparticles, J. Lumin. 209 (2019) 302–315.

[45] M. Mohapatra, B. Rajeswari, N.S. Hon, R.M. Kadam, Uranium luminescence in $La_2Zr_2O_7$: effect of concentration and annealing temperature, Luminescence 31 (8) (2016) 1519–1523.

[46] Z.H. Xu, Z.Y. Shen, R.D. Mu, L.M. He, Phase structure, thermophysical properties and thermal cycling behavior of novel $(Sm_{0.2}La_{0.8})_2(Zr_{0.7}Ce_{0.3})_2O_7$ thermal barrier coatings, Vacuum 157 (2018) 105–110.

[47] K.N. Woods, T.-H. Chiang, P.N. Plassmeyer, M.G. Kast, A.C. Lygo, A.K. Grealish, S.W. Boettcher, C.J. Page, High-κ lanthanum zirconium oxide thin film dielectrics from aqueous solution precursors, ACS Appl. Mater. Interfaces 9 (12) (2017) 10897–10903.

[48] D. Huo, G. Baldinozzi, D. Siméone, H. Khodja, S. Surblé, Grain size-dependent electrical properties of $La_{1.95}Sr_{0.05}Zr_2O_{7-\delta}$ as potential Proton Ceramic Fuel Cell electrolyte, Solid State Ion. 298 (2016) 35–43.

[49] B. Paul, K. Singh, T. Jaroń, A. Roy, A. Chowdhury, Structural properties and the fluorite–pyrochlore phase transition in $La_2Zr_2O_7$: the role of oxygen to induce local disordered states, J. Alloy. Comp. 686 (2016) 130–136.

[50] X. Xue, R.L. Penn, E.R. Leite, F. Huang, Z. Lin, Crystal growth by oriented attachment: kinetic models and control factors, CrystEngComm 16 (8) (2014) 1419–1429.

[51] G. Madras, B.J. McCoy, Temperature effects during Ostwald ripening, J. Chem. Phys. 119 (3) (2003) 1683–1693.

[52] G. Madras, B.J. McCoy, Temperature effects on the transition from nucleation and growth to Ostwald ripening, Chem. Eng. Sci. 59 (13) (2004) 2753–2765.

[53] D.R. Rittman, K.M. Turner, S. Park, A.F. Fuentes, C. Park, R.C. Ewing, W.L. Mao, Strain engineered pyrochlore at high pressure, Sci. Rep. 7 (1) (2017) 2236.

[54] B.-N. Kim, K. Hiraga, K. Morita, Kinetics of normal grain growth depending on the size distribution of small grains, Mater. Trans. 44 (11) (2003) 2239–2244.

[55] W.-N. Wang, W. Widiyastuti, T. Ogi, I.W. Lenggoro, K. Okuyama, Correlations between crystallite/particle size and photoluminescence properties of submicrometer phosphors, Chem. Mater. 19 (7) (2007) 1723–1730.

[56] Y. Zhang, J. Xu, Q. Cui, B. Yang, Eu^{3+}-doped $Bi_4Si_3O_{12}$ red phosphor for solid state lighting: microwave synthesis, characterization, photoluminescence properties and thermal quenching mechanisms, Sci. Rep. 7 (2017) 42464.

[57] N.S. Singh, R.S. Ningthoujam, N. Yaiphaba, S.D. Singh, R.K. Vatsa, Lifetime and quantum yield studies of Dy^{3+} doped $GdVO_4$ nanoparticles: concentration and annealing effect, J. Appl. Phys. 105 (6) (2009) 064303.

[58] L. González-Reyes, I. Hernández-Pérez, L.D.-B. Arceo, H. Dorantes-Rosales, E. Arce-Estrada, R. Suárez-Parra, J. Cruz-Rivera, Temperature effects during Ostwald ripening on structural and bandgap properties of TiO_2 nanoparticles prepared by sonochemical synthesis, Mater. Sci. Eng., B 175 (1) (2010) 9–13.

[59] X. Jiang, W. He, X. Zhang, Y. Wu, Q. Zhang, G. Cao, H. Zhang, J. Zheng, T.R. Croley, J.-J. Yin, Light-induced assembly of metal nanoparticles on ZnO enhances the generation of charge carriers, reactive oxygen species, and antibacterial activity, J. Phys. Chem. C 122 (51) (2018) 29414–29425.

[60] X. Qin, X. Liu, W. Huang, M. Bettinelli, X. Liu, Lanthanide-Activated phosphors based on 4f-5d optical transitions: theoretical and experimental aspects, Chem. Rev. 117 (5) (2017) 4488–4527.

[61] K. Kaviyarasu, E. Manikandan, Z.Y. Nuru, M. Maaza, Quantum confinement of lead titanate nanocrystals by wet chemical method, J. Alloy. Comp. 649 (2015) 50–53.

[62] S.K. Gupta, K. Sudarshan, P. Ghosh, A. Srivastava, S. Bevara, P. Pujari, R. Kadam, Role of various defects in the photoluminescence characteristics of nanocrystalline $Nd_2Zr_2O_7$: an investigation through spectroscopic and DFT calculations, J. Mater. Chem. C 4 (2016) 4988–5000.

[63] N.S. Singh, R. Ningthoujam, N. Yaiphaba, S.D. Singh, R. Vatsa, Lifetime and quantum yield studies of Dy^{3+} doped $GdVO_4$ nanoparticles: concentration and annealing effect, J. Appl. Phys. 105 (6) (2009) 064303.

[64] W.-N. Wang, W. Widiyastuti, T. Ogi, I.W. Lenggoro, K. Okuyama, Correlations between crystallite/particle size and photoluminescence properties of submicrometer phosphors, Chem. Mater. 19 (2007) 1723–1730.

[65] L. Vradman, J. Zana, A. Kirschner, M. Herskowitz, Synthesis of $LaMnO_3$ in molten chlorides: effect of preparation conditions, Phys. Chem. Chem. Phys. 15 (26) (2013) 10914–10920.

[66] P. Afanasiev, C. Geantet, Synthesis of solid materials in molten nitrates, Coord. Chem. Rev. 178–180 (1998) 1725–1752.

[67] X. Wu, Y. Liang, M. Liu, R. Chen, Y. Li, Synthesis and fluorescence properties of Y_2O_3:Eu by molten salt synthesis method, J. Rare Earths 28 (5) (2010) 688–692.